remote sensing

MDPI

Article

Multisource Remote Sensing Identification and Analysis of Slow-Moving Landslides Associated with the July 2023 Extreme Rainfall Event in Fangshan and Mentougou Districts, Beijing

Xiaoyi Wang [1], Debao Yuan [1,*], Yueze Zheng [2], Bo Zhao [2] and Jiaqi Li [2]

[1] College of Geoscience and Surveying Engineering, China University of Mining and Technology (Beijing), Ding 11 Xueyuan Road, Haidian District, Beijing 100083, China; sqt2400204099@student.cumtb.edu.cn
[2] Beijing Institute of Surveying and Mapping, 15 Yangfangdian Lu, Beijing 100080, China; zhengyueze@bjschsjyjy.wecom.work (Y.Z.); zhaobo@bjschsjyjy.wecom.work (B.Z.); lijiaqi@bjschsjyjy.wecom.work (J.L.)
* Correspondence: yuandb@cumtb.edu.cn

Highlights

What are the main findings?

- We combined pre- and post-event optical images into six input channels for U-Net to map event-related shallow landslides. On the shared validation set, F1-score rose by 3.05 percentage points and intersection over union (IoU) by 5.28 points.
- We used InSAR to map pre-existing landslides and screen their activity during the first six months after the event. The six-month screen identified acceleration at 50 CA landslides and renewed motion at 15 PS landslides. The other 37 did not meet either criterion.

What are the implications of the main findings?

- We observed faster or renewed deformation at some pre-existing landslides after the extreme rainfall event. These changes highlight the need for continued deformation monitoring after extreme rainfall.
- The complementary use of optical imagery, time-series InSAR, and airborne LiDAR provides integrated evidence for event-related landslide mapping, historical deformation tracking, and concealed landslide geomorphic interpretation.

Abstract

We combined Sentinel-1 time series, bitemporal optical imagery, and airborne LiDAR data to examine landslide activity around the July 2023 extreme rainfall event in Fangshan and Mentougou Districts, Beijing. Pre-event interpretation identified 102 slow-moving landslides covering approximately 6.59 km^2. Among them, 86 showed continuous activity, while 16 showed a trend toward stabilization after earlier activity. Across three runs, the six-channel U-Net achieved mean validation precision, recall, F1-score, and intersection over union (IoU) of 94.09%, 94.18%, 94.13%, and 88.91%, respectively. Compared with the post-event-only model, mean F1-score and IoU increased by 3.05 and 5.28 percentage points, respectively. After manual visual review, the regional inventory contained 13,534 event-related shallow landslides covering approximately 6.77 km^2. Screening during the first six post-event months identified acceleration at 50 pre-existing landslides and renewed motion at 15. The remaining 37 fell into the Other category. Four cases illustrate local changes in line-of-sight deformation. Time-series interferometric synthetic aperture radar (InSAR), bitemporal optical imagery, and LiDAR provide complementary information on pre-event activity, event-related surface damage, and post-event deformation. Together, these data support a more comprehensive understanding of landslide activity evolution, landslide

Check for updates

Academic Editors: Jingze Li, Yakun Han and Giuseppe Casula

Received: 2 November 2026
Revised: 20 November 2026
Accepted: 23 November 2026
Published: 27 November 2026

Copyright: © 2026 by the authors. Licensee MDPI, Basel, Switzerland. This article is an open access article distributed under the terms and conditions of the Creative Commons Attribution (CC BY) license.

hazard identification, rapid post-disaster mapping, and continued activity monitoring in mountainous areas.

Keywords: slow-moving landslides; InSAR; LiDAR; landslide reactivation; July 2023 extreme rainfall

1. Introduction

Against the backdrop of global climate change, extreme precipitation events are becoming more frequent and intense, increasing the risk of landslides, rockfalls, and related mountain hazards [1,2]. The mountainous areas of northern China have rugged terrain and complex geological settings. Sustained heavy rainfall can trigger widespread slope failures in these areas. In July 2023, Beijing experienced an exceptionally severe rainstorm influenced by Typhoon Doksuri. Fangshan and Mentougou Districts suffered particularly severe impacts, with numerous landslides and rockfalls [3–5]. However, extreme rainfall does not exclusively produce newly formed shallow failures. Some slopes may have undergone slow deformation for years before the event, whereas other existing landslides may have gradually become less active and subsequently stabilized before being reactivated during extreme rainfall [6,7]. Consequently, landslide inventories based solely on post-event surface damage cannot reconstruct pre-event activity. They also cannot fully capture the progression from slow pre-event deformation to rapid event-related responses and continued post-event movement.

Remote sensing provides tools for regional landslide identification and dynamic monitoring. High-resolution optical imagery provides broad spatial coverage and readily interpretable surface information for delineating landslide boundaries, detecting changes between pre- and post-event conditions, and rapidly mapping post-disaster damage [8]. Advances in deep-learning semantic segmentation have improved automated landslide extraction from optical imagery [9–13]. Time-series interferometric synthetic aperture radar (InSAR) can detect surface displacements at millimeter-to-centimeter scales, making it valuable for identifying long-term slow-moving landslides and analyzing their deformation histories [14,15]. Light detection and ranging (LiDAR) point clouds provide high-resolution topographic information with reduced obstruction from vegetation, supporting the recognition of head scarps, lateral boundaries, deposits, and internal microtopographic features [16–18]. In recent years, integrating multisource remote sensing data has become an important approach to identifying and analyzing complex landslides [19,20]. However, these data sources capture different aspects of landslides: optical imagery is particularly sensitive to event-related surface damage, time-series InSAR focuses on sustained surface deformation, and LiDAR resolves fine-scale landslide morphology [21]. A single source is therefore rarely sufficient to determine whether a slope was active before an event, what changed during the disaster, and whether deformation continued afterward.

Previous multisource studies combined different observations to delineate suspected landslides and describe their shape and movement [22]. Ma and Wang [5] used pre- and post-event optical images to map event-related shallow landslides after the July 2023 rainfall in Beijing. Their inventory shows where the event affected the ground surface. Here we ask whether pre- and post-event line-of-sight (LOS) histories can distinguish acceleration of continuous movement from renewed motion on pre-existing slopes. We examine the July 2023 extreme rainfall event in Fangshan and Mentougou Districts, Beijing. We use Sentinel-1 observations to track slope activity before and after the event. Paired Beijing-2 images support shallow landslide mapping, and airborne LiDAR supports the interpretation of concealed landslides.

2. Materials and Methods

2.1. Study Area

The study area includes Fangshan and Mentougou Districts in southwestern Beijing, China. Fangshan covers approximately 2019 km^2 [23] and Mentougou approximately 1447.85 km^2 [24], giving a combined area of 3466.85 km^2. This region in western Beijing is prone to geological hazards [25]. The terrain is generally higher in the northwest and lower in the southeast. The landforms change from low- and middle-elevation mountains and hills in the northwest to alluvial plains and floodplains near the mountain front in the southeast [26,27]. The northwest has long mountain ranges, many valleys, and steep slopes with deep erosion. In contrast, the southeast is relatively flat. It mainly consists of alluvial plains and floodplains formed by the Yongding and Dashi Rivers, with clear sediment deposits near the mountain front. Mountains cover much of the study area. Slope angles vary widely, and land cover is complex. Tectonic activity, differences in rock types, rainfall erosion, and human engineering activities also affect some parts of the region. Together, these conditions favor the occurrence of landslides and rockfalls [28]. Figure 1 shows the study area and remote sensing data coverage.

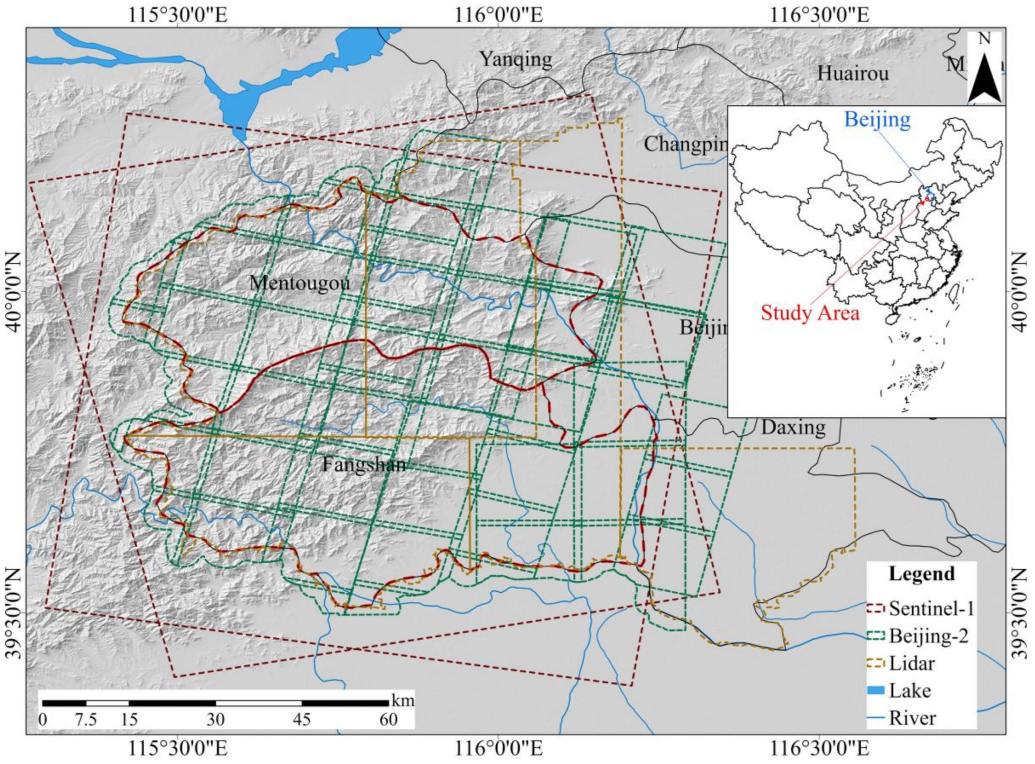

Figure 1. Administrative boundaries of Fangshan and Mentougou Districts, Beijing, and coverage of Sentinel-1, Beijing-2 optical imagery and airborne LiDAR.

Zhaitang in western Mentougou illustrates the geological diversity of the mountainous study area. Carbonate rocks, sandstone, and volcanic rocks occur locally, while loess and loose deposits cover parts of the slopes and valleys [29]. Widespread bedrock joints, faults, and valley incision create complex slope structures. Loose surface deposits and unfavorable discontinuities may provide conditions for continued slow slope deformation.

2.2. Extreme Rainfall Event

In July 2023, the remnants of Typhoon Doksuri, the subtropical high, and orographic uplift jointly contributed to extreme rainfall across northern China [30,31]. This rainfall caused the "23·7" major flood in the Haihe River Basin [32]. Beijing experienced 83 h of

heavy rainfall from 20:00 on 29 July to 07:00 on 2 August. Mean rainfall reached approximately 331 mm across Beijing and 538 mm and 599 mm in Mentougou and Fangshan Districts, respectively [33]. Station records show that the 2023 maximum consecutive five-day precipitation reached 347.29 mm at Mentougou station during 27–31 July. Fangshan station recorded 322.15 mm during 29 July–2 August [34].

2.3. Data

To identify pre-event slow-moving landslides, rapidly occurring shallow landslides during the disaster, and slopes with continued post-event movement, we combine several datasets. These include high-resolution optical imagery, Sentinel-1 SAR images, SRTM DEM, airborne LiDAR point clouds, and rainfall records from weather stations. These data complement each other in temporal coverage, spatial resolution, and the features they capture. Table 1 shows their sources, acquisition methods, and main parameters.

The Beijing-2 images were acquired on 12 March and 3 August 2023, with 55 scenes for each date. Their nominal pixel spacing is 0.5 m. The co-registration residual is 0.75 m, equivalent to 1.5 nominal pixels. Both dates used common ground control, terrain data, and orthorectification. The optical footprint defines regional U-Net mapping.

We used Sentinel-1 IW SLC data from ascending Path 142 for SBAS-InSAR analysis [35]. The archived LOS deformation histories contain 295 observation dates, including 216 pre-event and 79 post-event dates.

Airborne point clouds acquired on 15 August 2023 were supplied by Beijing Dichi Technology Co., Ltd. (Beijing, China). The survey covered approximately 1812 km^2, including 1347 km^2 in Fangshan and 465 km^2 in Mentougou. The DEM used a 2 m grid in WGS 84 and had a reported vertical accuracy of 0.35 m.

Table 1. Remote sensing and ancillary data used in this study.

Data Type	Data Product/ Platform	Acquisition Period	Data Product	Key Parameters	Scenes/ Density	Data Source/ Acquisition
Optical imagery	Beijing-2	12 March 2023 and 3 August 2023	RGB imagery	0.5 m source product	Two dates; 55 scenes for each date	Beijing-2 satellite imagery service [36]
Radar imagery	Sentinel-1	July 2015–July 2023 and August 2023–April 2026	IW-mode SLC products	C-band; Ascending Path 142	295 observation dates	Copernicus Data Space Ecosystem [37]
DEM	SRTM DEM	-	Digital elevation model	30 m	1 data collection	USGS EarthExplorer [38]
Point clouds	CountryMapper-2	15 August 2023	Airborne LiDAR point clouds	2 m	8 points/m^2	Beijing Dichi Technology Co., Ltd.
Precipitation	Mentougou and Fangshan stations	2014–2024	Daily precipitation	1 d	2 stations	National Meteorological Science Data Center [34]

2.4. Overall Workflow

We developed a multisource remote sensing workflow to identify landslides and analyze activity changes around the "23·7" extreme rainfall event. The workflow covers the pre-event history, event observations, and continued post-event activity. The datasets cap-

ture long-term deformation, event-related surface disturbance, and detailed landforms. We examine activity changes through spatial association and time-series comparisons. First, we analyzed multitemporal Sentinel-1 SAR observations from July 2015 to July 2023 using SBAS-InSAR to obtain pre-event LOS rates and cumulative displacement histories. We combined these results with high-resolution optical imagery and terrain data to manually delineate pre-existing landslides showing continued slow deformation or earlier activity. Based on their pre-event displacement histories, we classified them as continuously active (CA) or previously active with a trend toward stabilization (PS). We then prepared three-channel post-event inputs and six-channel bitemporal inputs for U-Net using Beijing-2 optical imagery with a nominal pixel spacing of 0.5 m. We compared segmentation performance using the same training and validation split. We applied area filtering and manual visual review to the regional six-channel predictions to compile an event-related shallow landslide inventory. We also used Sentinel-1 time-series InSAR results from August 2023 to April 2026 to track post-event slope activity. We compared displacement and fitted rates during the pre-event year and first six post-event months to screen all 102 pre-existing landslides for acceleration and renewed motion. Within the airborne LiDAR coverage, we used the bare-earth DEM and terrain products to interpret concealed landslide morphology and refine boundaries obscured by vegetation. Finally, we spatially linked pre-event deformation histories, event-related optical changes, post-event deformation, and LiDAR landforms. We combined this evidence with LOS displacement and kinematic curves from four cases to examine activity changes and the complementary roles of the datasets. Figure 2 shows the workflow.

2.5. Landslide Identification Methods

2.5.1. Slow-Moving Landslide Identification Using Time-Series InSAR

We used GAMMA software (version 20231211; GAMMA Remote Sensing AG, Gümligen, Switzerland) and the small baseline subset interferometric synthetic aperture radar (SBAS-InSAR) method [39–41] to estimate LOS deformation rates and cumulative displacement histories.The software was purchased by the Beijing Institute of Surveying and Mapping. All 295 Sentinel-1 scenes from ascending Path 142 during 2015–2026 were entered into a single time-series analysis. We used the first acquisition, dated 30 July 2015, as the co-registration reference image. We first clipped the single-look complex images to the study area, applied precise orbit corrections, and co-registered the images. We used 10 × 2 multilooking to reduce phase noise. To balance interferometric quality and long-term network connectivity, we selected candidate pairs using maximum temporal and spatial baselines of 120 days and 1000 m, respectively.

After generating differential interferograms, we visually inspected each for fringe continuity, coherence, and anomalous interference. We removed pairs with clear decorrelation or poor interferometric quality. We also checked connections between acquisitions to maintain network connectivity and avoid isolated images. We retained 385 interferograms for time-series inversion. Processing used a coherence threshold of 0.4, together with interferogram quality checks to control the influence of low-quality observations. We used the SRTM DEM to remove topographic phase, then filtered and unwrapped the interferograms for SBAS time-series analysis.

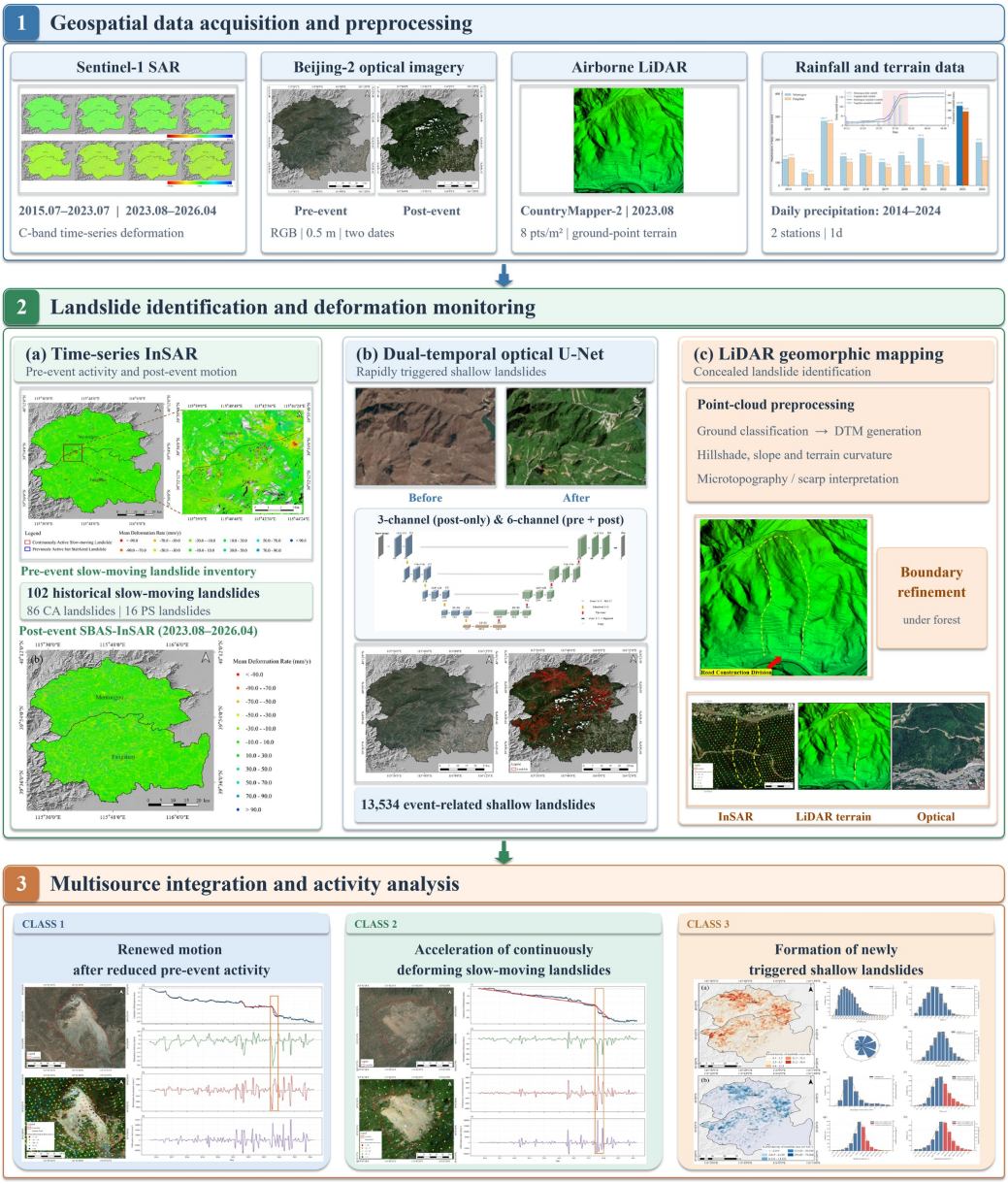

Figure 2. Workflow for multisource landslide identification and activity analysis.

We selected a relatively stable reference area with concentrated urban buildings, avoiding locations with clear deformation. A stable point within this area provided the relative displacement reference. We used high- and low-pass filtering to estimate and suppress atmospheric delays. We masked deforming areas to reduce the influence of actual deformation on atmospheric-error estimation. Using the screened interferometric network, we applied singular value decomposition to estimate LOS deformation rates for each observation interval. We accumulated interval displacements to obtain displacement histories and then geocoded the results.

We located candidate slopes on geocoded pre-event LOS deformation maps. We checked the spatial continuity of deformation points against optical imagery and terrain data, then manually delineated landslide boundaries. We interpreted pre-event activity from LOS displacement histories at coherent points in the upper depleted sector. We classified slopes as continuously active (CA) where same-direction displacement continued accumulating during the final pre-event year, including movement at an approximately constant rate. We assigned the previously active with a trend toward stabilization (PS) class

where earlier accumulation gave way to nearly flat curves with little further same-direction displacement. Interpretation considered each slope's deformation history and used no uniform numerical threshold.

2.5.2. Detection of Event-Related Shallow Landslides from Optical Imagery

Optical remote sensing imagery reveals exposed ground, boundary changes, and vegetation disturbance before and after extreme rainfall. These images provide an important data source for post-event mapping and pixel-level identification of rapidly occurring shallow landslides [42]. U-Net uses an encoder–decoder architecture to extract multiscale features and restore spatial resolution for pixel-wise classification [43]. Researchers widely use U-Net for landslide detection in optical imagery [44]. Bitemporal images combine pre-event background information with post-event disturbance information. This combination highlights newly exposed areas, boundary changes, and vegetation damage more clearly than single-date imagery [45].

We used a U-Net model to identify rapidly occurring shallow landslides and compared two input configurations. The three-channel model used post-event RGB imagery from time T_2. For the six-channel model, we geometrically corrected and co-registered the pre-event T_1 and post-event T_2 RGB images. We then concatenated these images along the channel dimension to form the six-channel input. Their inputs are expressed as follows:

$$X_3 = I_2 \in \mathbb{R}^{HxWx3} \quad (1)$$

$$X_6 = concat(I_1, I_2) \in \mathbb{R}^{HxWx6} \quad (2)$$

where X_3 and X_6 denote the three- and six-channel input samples, respectively; I_1 and I_2 are the pre- and post-event RGB images; H and W are the patch height and width; and concat(,) denotes channel-wise concatenation. Both experiments used the same U-Net architecture and differed only in the number of input channels. This setup allowed us to assess the effect of bitemporal information on landslide identification accuracy.

We converted manually delineated landslide polygons near the Fangshan–Mentougou boundary into binary masks. We cropped the paired Beijing-2 images and masks into 256 × 256 pixel tiles. We randomly divided the same local dataset into 1456 training tiles and 318 validation tiles. Checks of their geographic footprints found no duplicate tiles or positive-area overlap.

Both models were trained for 200 epochs with a batch size of 8 and an initial learning rate of 10^{-4}. The archived implementation uses AdamW (weight decay 10^{-5}) and an IoU-monitored ReduceLROnPlateau schedule with factor 0.5, patience of six epochs and minimum learning rate of 10^{-6}. Both models use BCEWithLogitsLoss and Dice loss with weights of 0.2 and 0.8, respectively, plus normalization and random horizontal and vertical flips. Each U-Net has four pooling and upsampling stages, skip connections and 64 initial feature channels. The experiments ran in Python with PyTorch 2.1.0 on an Intel Core i9-14900KF and NVIDIA RTX 4090. We ran the two additional seeds on an NVIDIA RTX 4090 using PyTorch 2.1.0. All runs used the same hyperparameters and data split. The three-channel runs retained mixed precision, and six-channel runs retained single precision.

For each model, we compared pixel predictions with reference masks on all 318 validation patches. We pooled true positives (TP), false positives (FP), false negatives (FN) and true negatives (TN) across patches before calculating the following metrics.

$$Precision = \frac{TP}{TP + FP} \quad (3)$$

$$Recall = \frac{TP}{TP + FN} \quad (4)$$

$$F1 = \frac{2 \times Precision \times Recall}{Precision + Recall} \quad (5)$$

$$IoU = \frac{TP}{TP + FP + FN} \quad (6)$$

Precision describes the proportion of predicted landslide pixels that match the reference. Recall describes the proportion of reference landslide pixels the model detects. The F1-score summarizes precision and recall. Intersection over union (IoU) divides the shared area by the area of the union.

We applied the six-channel U-Net to regional mapping. We projected the raw prediction, area-filtered prediction, and final inventory to WGS 84/UTM zone 50N. We overlaid the filtered prediction and final inventory to count polygons without positive-area overlap. We dissolved the raw and final polygons separately and calculated shared area, exclusive areas, and area IoU (intersection area divided by union area).

2.5.3. Identification of Concealed Landslides Using Airborne LiDAR

Vegetation covers some pre-existing landslides in the study area. This makes their boundaries and internal microtopography difficult to identify in optical images. We therefore used airborne LiDAR for geomorphic interpretation and identification of concealed landslides. Laser returns provide three-dimensional information. Extracting ground returns and reconstructing the terrain can partly reduce the effect of vegetation cover [46]. LiDAR-derived high-resolution terrain data also reveal landslide landforms and help identify the boundaries of concealed landslides [47].

We classified ground points with the default Ground settings in Terrasolid TerraScan (Terrasolid Ltd., Espoo, Finland), using iterative TIN densification [48]. We generated a 2 m bare-earth DEM using TIN linear interpolation. We calculated local terrain measures for geomorphic interpretation within a 3 × 3 pixel neighborhood, approximately 6 m wide. Slope, curvature, and multidirectional hillshades aided interpretation.

We interpreted landslide boundaries from arcuate head scarps, flank breaks in slope or gullies, stepped or depressed internal terrain, and toe bulges or deposits [49]. We then cross-checked the LiDAR interpretation against optical imagery and time-series InSAR. Optical imagery showed land cover, gullies, roads, and human-made features. These observations helped us rule out non-landslide landforms with similar shapes. Time-series InSAR provided evidence of past or ongoing slow deformation. Together, these checks improved the interpretation of the concealed landslide.

2.6. Rainfall Summaries and Case-History Interpretation

We calculated the annual maximum consecutive five-day precipitation total separately for each station using Equation (7). The five days must all fall within the same calendar year. This station-scale daily index differs from the district-average 83 h event accumulation in Section 2.2.

$$Rx5day_y = max_{t \in T(y)} \left[\Sigma_{j=0...4} P(t+j) \right] \quad (7)$$

Here $P(t)$ is station precipitation on day t in mm, and $T(y)$ contains the valid start dates of five-day windows wholly within year y. Both stations had complete daily coverage in the input files for 2014–2024.

The post-event activity screen retained the original pre-event CA/PS classes. We compared net LOS displacement and fitted rates between the pre-event year (29 July 2022–28 July 2023) and first six post-event months (3 August 2023–2 February 2024). The screen included 25,157 measurement points with complete observations within the landslide boundaries. For CA slopes, we examined whether the magnitudes of the same-direction rate and net

displacement per unit time increased. For PS slopes, we examined whether detectable same-direction motion resumed after weak pre-event activity. The screen considered estimation errors and retained one classification outcome and a corresponding representative point for each landslide. Slopes meeting neither criterion entered the Other category. Table S2 provides the detailed criteria. We calculated net LOS displacement as the median of the last three observations minus the median of the first three observations within each window. We estimated signed LOS rates by fitting a straight line to all displacement observations against their actual acquisition dates within each window.

For the four plotted case points, we defined negative LOS rate enhancement, E, as the pre-event annual rate minus the post-event half-year rate. Positive E indicates a shift toward more negative post-event rates. The regression estimated separate intercepts and slopes for the two windows. We used a correlation-robust covariance estimator with a Bartlett kernel and a 36-day bandwidth based on actual date separations. We calculated 95% confidence intervals for E using the normal approximation and applied Holm correction across the four comparisons. This test describes statistical changes in fitted trends. Table S4 provides the detailed results. We selected one measurement point in the upper source area of each of the four representative landslides [50] to describe local LOS motion. Sampling intervals were mainly 12 days, with occasional gaps of up to 48 days.

The kinematic curves use a three-observation running median (M_3) and, for the displacement series, a local quadratic fit (Q_3). Velocity, acceleration and jerk are successive local linear slopes (L_3) fitted on the actual observation dates. We shift the fitting window inward at record ends and use the recorded dates across gaps without interpolating new observations.

Equations (8a)–(8d) define the four plotted quantities, and Equation (9) gives the local slope. Higher-order derivatives amplify short-period noise. We use them to describe local activity and use raw displacement observations to test changes in rate.

$$\tilde{d}_i = Q_3[M_3(d)]_i \tag{8a}$$

$$v_i = M_3[L_3(\tilde{d})]_i \tag{8b}$$

$$a_i = M_3[L_3(v)]_i \tag{8c}$$

$$j_i = M_3[L_3(a)]_i \tag{8d}$$

$$[L_3(f)]_i = \frac{\Sigma_j \in W_i\ (t_j - \bar{t}_i)(f_j - \bar{f}_i)}{\Sigma_j \in W_i\ (t_j - \bar{t}_i)^2} \tag{9}$$

Here d is cumulative LOS displacement (mm), t is elapsed time (yr), and W_i is the local three-observation window. Overbars indicate means within W_i. The units of v, a and j are mm yr^{-1}, mm yr^{-2} and mm yr^{-3}, respectively.

We assessed noise sensitivity using 3000 conditional perturbation simulations, retaining actual observation dates and the original smoothing and differentiation procedures. Noise scales came from seven-observation local quadratic residuals, assuming exponential temporal correlation with a 12-day timescale. We summarized each kinematic quantity using the median half-width of pointwise 95% perturbation intervals across the complete time series.

2.7. Spatial Summaries of Event-Related Shallow Landslides

We calculated planar kernel density in QGIS (version 3.44.15; QGIS Development Team, Open Source Geospatial Foundation) using the quartic point kernel, a 1000 m search radius and a 100 m output grid. We assigned each landslide point a weight of one for count density and a weight equal to the mapped polygon area in square meters for area

density. The study-area boundary constrained the search, and outputs were clipped to the study-area polygon. Densities are expressed per square kilometer.

$$K(x) = \frac{3 \times 10^6}{\pi h^2} \Sigma_{i \in I(x)} w_i [1 - (d_i(x)/h)^2]^2 \quad (10)$$

Equation (10) describes the quartic kernel density evaluated at raster cell center x [51]. Both h and d use meters. I(x) includes points within h that contribute under the boundary constraint. The factor 10^6 converts densities from per square meter to per square kilometer. The weight w is 1 for count density or polygon area in m^2 for area density.

We projected the elevation raster to a 27.31 m grid in WGS 84/UTM zone 50N (EPSG:32650) using bilinear interpolation. Equations (11) and (12) define relief, *TPI* and *TWI*.

$$Relief(x) = max_{W_r(x)} z - min_{W_r(x)} z,\ TPI(x) = z(x) - \bar{z}_{W_t(x)} \quad (11)$$

$$TWI(x) = ln\ [\frac{(F(x) + 1) \times 27.31255}{tan((\pi/180)\ max(\beta(x),\ 0.1))}] \quad (12)$$

Here z is elevation in meters, W_r is a 1000 × 1000 m rectangular window, and W_t is a centered 37 × 37-cell window (approximately 1.01 km wide). Mean elevation $\bar{z}$ is calculated over the valid cells in W_t. F is unweighted D8 continuous flow accumulation and β is slope in degrees. The tangent uses the slope lower bound of 0.1° after conversion to radians.

We used QGIS to calculate slope and aspect. We calculated profile and tangential curvature from quadratic surfaces using a fixed 27.31 m neighborhood [52]. Profile curvature follows the slope line and tangential curvature is tangent to the contour. We extracted terrain values at a representative point inside each polygon to summarize landslide counts and polygon-area shares. We grouped elevation, slope and relief in 100 m, 5° and 50 m intervals, respectively, with eight aspect sectors. Interior TWI breaks were 3, 4, 5, 6, 7, 8, 9, 10, 12 and 14. Signed TPI and curvature classes used 25 m and 0.0025 intervals, respectively, between −150 and 150 m for TPI and −0.015 and 0.015 for curvature.

For each terrain class, we calculated the share of mapped shallow landslides and the share of valid terrain in the optical mapping area. Table S3 reports the ratio of these shares.

3. Results

3.1. Time-Series InSAR Monitoring and Landslide Identification Results

3.1.1. Characteristics of InSAR-Derived Deformation

We derived mean deformation rates before and after the '23·7' extreme rainfall event using Sentinel-1 SBAS-InSAR time series (Figure 3). The pre-event period covered July 2015–July 2023, while the post-event period covered August 2023–April 2026. We used the same deformation-rate classes and color scheme for both periods to facilitate spatial comparison.

Before the event, mean LOS deformation rates across the study area ranged from approximately −120 to 100 mm/year. Most areas showed relatively small deformation. Clear, spatially continuous deformation zones mainly occurred in the western mountains. These zones included western and northwestern Mentougou, western Fangshan, and the Fangshan–Mentougou boundary area. Some anomalies extended along valley sides and mountain slopes, indicating that certain slopes were already moving slowly before the '23·7' event. After the event, mean LOS deformation rates ranged from approximately −178 to 186 mm/year. Spatial variability was greater than before the event. Some pre-event deformation anomalies persisted in western Mentougou and along the Fangshan–Mentougou boundary. In central-western and western Fangshan, some local anomalies increased in deformation magnitude or spatial extent. These results suggest that changes in

slope activity varied across the study area. Further assessment of individual slopes requires examining their pre-event displacement histories and continuing post-event monitoring.

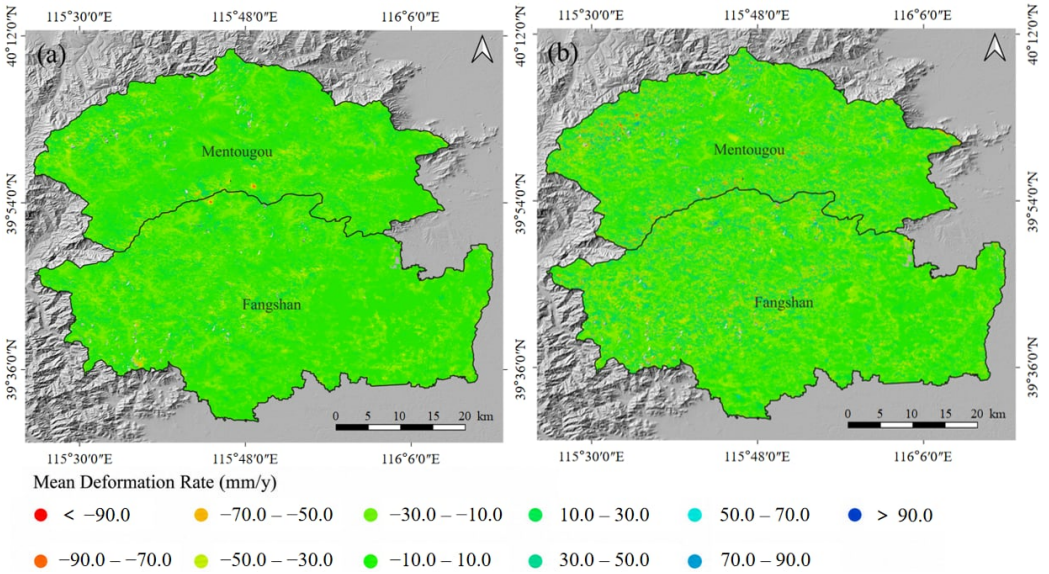

Figure 3. Spatial distribution of mean line-of-sight (LOS) deformation rates before and after the July 2023 extreme rainfall event: (**a**) pre-event period; (**b**) post-event period.

3.1.2. Inventory and Spatial Characteristics of Pre-Event Slow-Moving Landslides

The interpreted inventory contains 102 pre-event slow-moving landslides covering approximately 6.59 km^2. The original interpretation assigned 86 landslides to CA and 16 to PS (Table S1). Fangshan contained 82 inventoried landslides (80.39%) covering 3.62 km^2, and Mentougou contained 20 (19.61%) covering 2.98 km^2. Mean mapped areas were 0.04 and 0.15 km^2 (Table 2), respectively.

Table 2. Number and area of pre-event slow-moving landslides.

Metric	Total	Activity Class		Administrative District	
		Continuously Active Slow-Moving Landslides	Previously Active Landslides Showing a Trend Toward Stabilization	Mentougou	Fangshan
Number	102	86	16	20	82
Share by count (%)	100	84.31	15.69	19.61	80.39
Total area (km^2)	6.59	5.87	0.72	2.98	3.62
Share by area (%)	100	89.01	10.99	45.14	54.86
Mean area (km^2)	0.06	0.07	0.05	0.15	0.04
Maximum area (km^2)	1.11	1.11	0.21	1.11	0.37

The 102 slow-moving landslides occur mainly along valleys and steep slopes in both districts, with a cluster near the Fangshan–Mentougou boundary (Figure 4). Individual landslides had mean elevations of about 175–1863 m and mean slopes of about 11–45°. The overall mean slope was about 31°.

The six-month screen identified acceleration at 50 CA landslides and renewed motion at 15 PS landslides. The other 37 did not meet either criterion. Table S2 reports all 102 results.

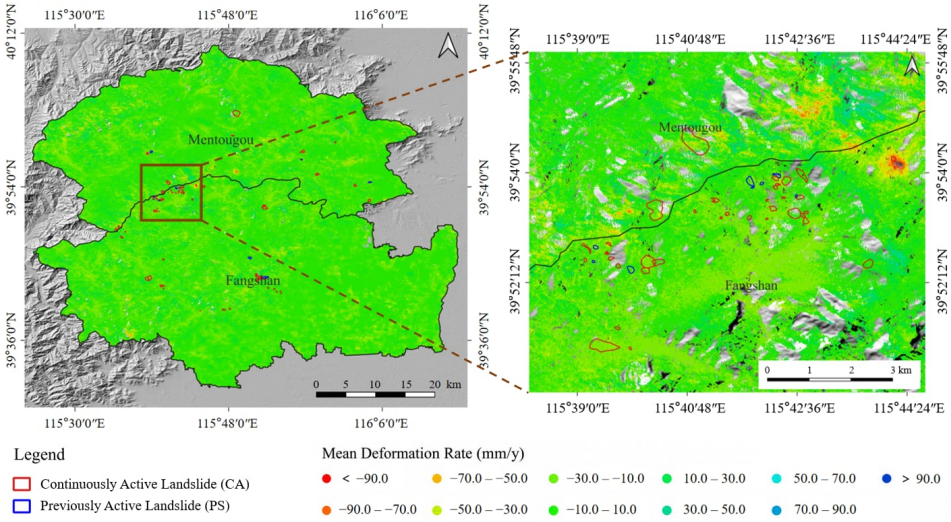

Figure 4. Spatial distribution of slow-moving landslides during the pre-event monitoring period: overview (**left**) and enlarged view (**right**).

3.2. Optical Mapping of Event-Related Shallow Landslides

3.2.1. U-Net Performance with Different Temporal Inputs

Figure 5 shows all training and validation curves for seeds 42, 123, and 456. Each run used 200 epochs, giving six runs overall. We selected each checkpoint by global validation IoU. Table 3 reports each seed and the mean and sample standard deviation. Mean six-channel precision, recall, F1-score, and IoU reached 94.09%, 94.18%, 94.13%, and 88.91%. The corresponding three-channel means were 89.36%, 92.88%, 91.09%, and 83.63%. Mean F1-score and IoU increased by 3.05 and 5.28 percentage points. Figure 5 shows loss and validation curves for all six runs.

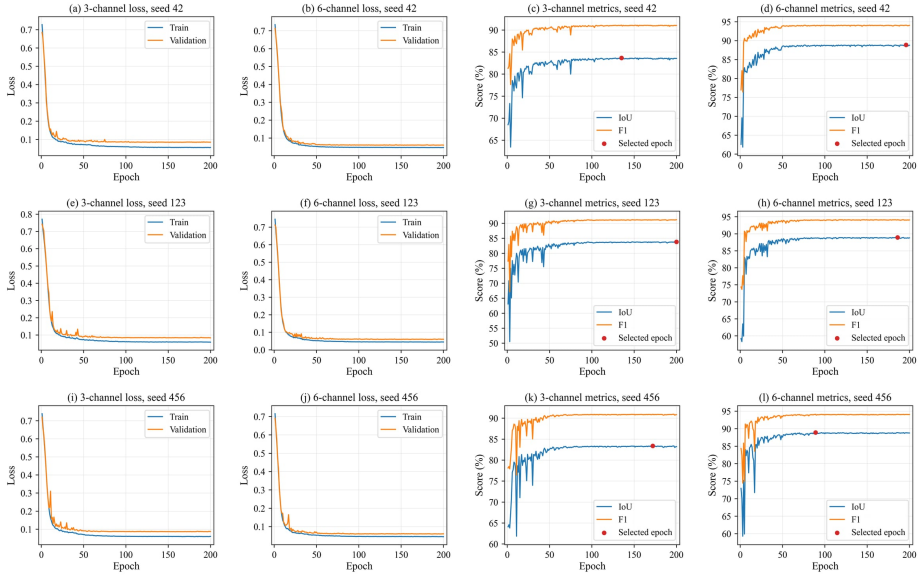

Figure 5. U-Net training and validation curves for three random seeds. (**a**) Three-channel loss, seed 42; (**b**) six-channel loss, seed 42; (**c**) three-channel validation IoU and F1-score, seed 42; (**d**) six-channel validation IoU and F1-score, seed 42; (**e**) three-channel loss, seed 123; (**f**) six-channel loss, seed 123; (**g**) three-channel validation IoU and F1-score, seed 123; (**h**) six-channel validation IoU and F1-score, seed 123; (**i**) three-channel loss, seed 456; (**j**) six-channel loss, seed 456; (**k**) three-channel validation IoU and F1-score, seed 456; (**l**) six-channel validation IoU and F1-score, seed 456. Red markers indicate the selected epochs.

Table 3. Validation performance of shallow landslide identification using different input configurations.

Input/Seed/Epoch	Precision	Recall	F1	IoU
3 ch/42/135	89.27%	93.04%	91.11%	83.68%
6 ch/42/196	93.93%	94.31%	94.12%	88.89%
3 ch/123/200	89.51%	92.97%	91.21%	83.83%
6 ch/123/186	94.29%	93.99%	94.14%	88.93%
3 ch/456/172	89.31%	92.63%	90.94%	83.38%
6 ch/456/89	94.03%	94.23%	94.13%	88.92%
3 ch mean ± SD	89.36 ± 0.13%	92.88 ± 0.22%	91.09 ± 0.14%	83.63 ± 0.23%
6 ch mean ± SD	94.09 ± 0.19%	94.18 ± 0.17%	94.13 ± 0.01%	88.91 ± 0.02%

Season, lighting, and viewing geometry may affect bitemporal model performance. The three seeds measure variation in random training on a fixed data split.

Because the six-channel model performed better across all four metrics, we used its predictions for regional mapping of rapidly occurring shallow landslides. To assess spatial detection errors, we compared the model predictions with landslide polygons verified through an independent manual review. Figure 6 shows pre- and post-event images and the spatial distribution of prediction errors in representative areas.

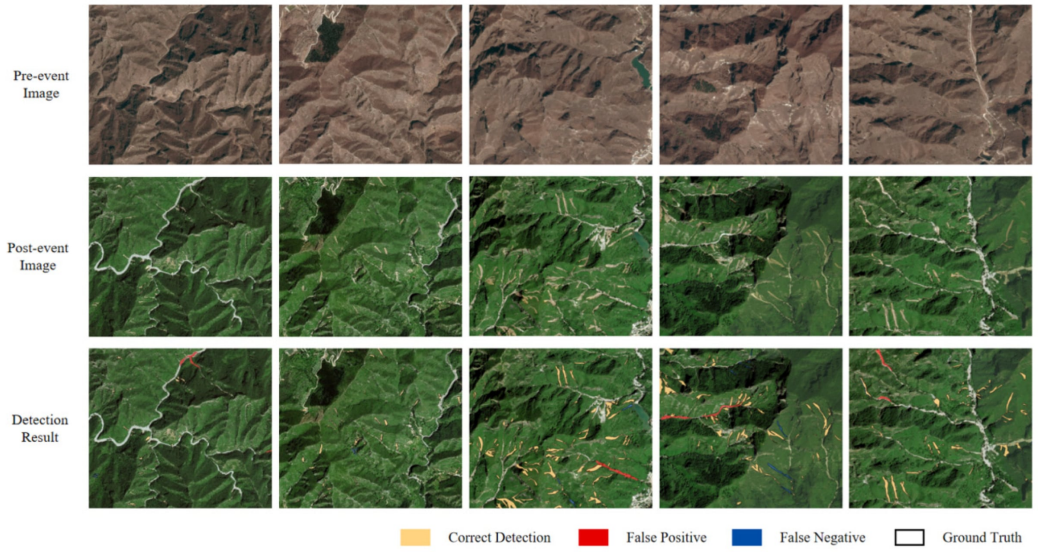

Figure 6. Comparison of correctly identified, false-positive, and false-negative shallow landslide regions in five representative areas.

In the selected areas, the model generally traced clearly exposed landslide scars. False positives commonly occurred on roads, channels, existing bare ground, shadows and disturbed land. Small, poorly defined or partly covered scars accounted for many omissions. During manual review, we corrected visible boundary and classification errors.

The raw six-channel U-Net prediction contained 32,802 polygons covering 7.100 km^2. The 10 m^2 minimum mapping unit removed 18,576 polygons and retained 14,226. After manual visual review, the final inventory contained 13,534 polygons covering 6.774 km^2. After filtering, 765 retained predictions had no positive-area overlap with the final inventory, and 77 final polygons had no positive-area overlap with the retained predictions. The full raw prediction and final inventory shared 6.712 km^2, yielding an area IoU of 93.73%. The shared area accounted for 94.55% of the prediction and 99.09% of the inventory. Prediction-only and inventory-only areas were 0.387 and 0.062 km^2, respectively (Figure 7).

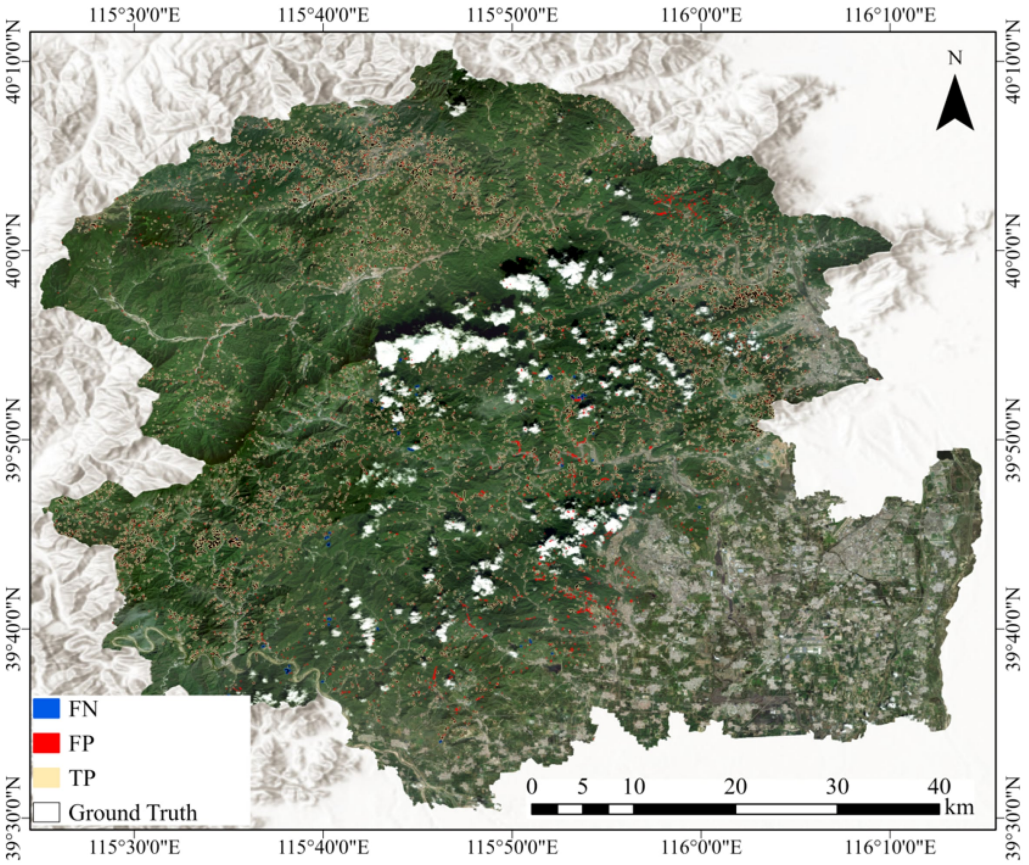

Figure 7. Regional comparison of the raw six-channel U-Net prediction and the manually reviewed shallow-landslide inventory.

3.2.2. Spatial Distribution of Event-Related Shallow Landslides

Figure 8 shows the pre- and post-event optical imagery and final inventory. The center column shows the landslide distribution across the study area, while the left and right columns show enlarged views of representative areas A and B.

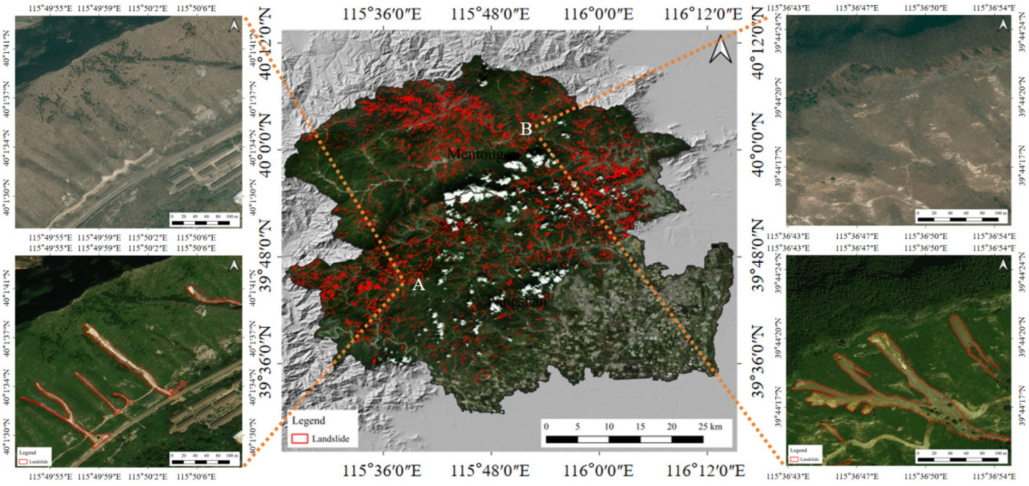

Figure 8. Pre-event imagery, post-event imagery, and mapped rapidly occurring shallow landslides across the study area. The central map shows the regional inventory. The left and right columns show areas A and B, respectively, with pre-event imagery above post-event imagery in each column.

New shallow landslides occurred as patches and elongated strips, primarily in rugged mountainous areas with well-developed valleys and strongly dissected slopes. In representative area A, newly exposed landslide scars were distinct, with relatively sharp boundaries, and the inventory captured their spatial forms reasonably well. Area B had a complex background of roads, buildings, and existing bare ground. These features resembled landslides in tone and texture, complicating the interpretation of some boundaries and requiring joint inspection of pre- and post-event imagery.

3.3. Geomorphic Identification of Concealed Landslides Using Airborne LiDAR

We used airborne LiDAR terrain products to assist the interpretation of a representative slope with dense vegetation and poorly defined optical boundaries. In satellite optical imagery, continuous vegetation cover makes the slope difficult to distinguish from surrounding natural hillsides in color and texture. No clearly continuous landslide boundary is apparent. InSAR records contain deformation observations within the slope, but the point distribution and limited spatial continuity do not allow reconstruction of the full landslide outline from InSAR alone.

Figure 9 compares time-series InSAR observations, LiDAR-derived terrain data, and satellite optical imagery for a representative concealed historical landslide. The LiDAR terrain model reveals the landslide's overall morphology more clearly. A relatively continuous arcuate break in slope is visible near the upper slope, with conspicuous changes in gradient and surface form. We interpret this feature as the head scarp. Some parts of the lateral boundaries appear as breaks in slope, sometimes alongside gullies, and contrast with the smoother surrounding hillside. One lateral boundary is relatively clear, whereas the other is less continuous. The interior exhibits heterogeneous microtopography with gullies, breaks in slope, and irregular relief, making its surface more complex than that of the surrounding natural slopes. The head scarp, partial lateral boundaries, and internal features together define a coherent landslide geomorphic unit.

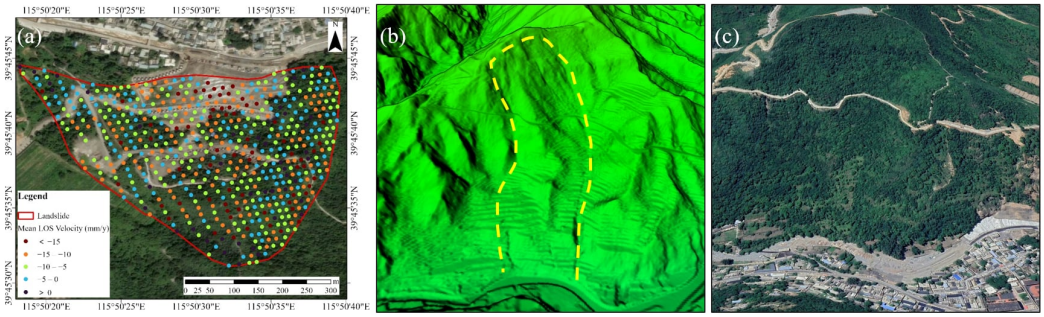

Figure 9. Multisource interpretation of a representative concealed landslide: (**a**) interferometric synthetic aperture radar (InSAR) deformation observations, where colored points represent mean LOS velocity classes (mm/yr), as indicated in the legend, and the red solid outline marks the landslide boundary; (**b**) light detection and ranging (LiDAR)-derived terrain, where the yellow dashed line marks the interpreted landslide boundary; (**c**) optical imagery.

The LiDAR terrain model helped trace landforms where vegetation obscured optical features and InSAR points lacked spatial continuity. A single LiDAR survey documents morphology. Assessment of current activity requires time-series observations.

3.4. Rainfall and LOS Deformation in the Selected Cases

3.4.1. Station Rainfall

Mentougou and Fangshan stations both recorded several days of heavy rain during the July 2023 event (Figure 10). The maximum five-day totals in 2023 were 347.29 mm at Mentougou (27–31 July) and 322.15 mm at Fangshan (29 July–2 August). Both were the highest in the respective station records for 2014–2024.

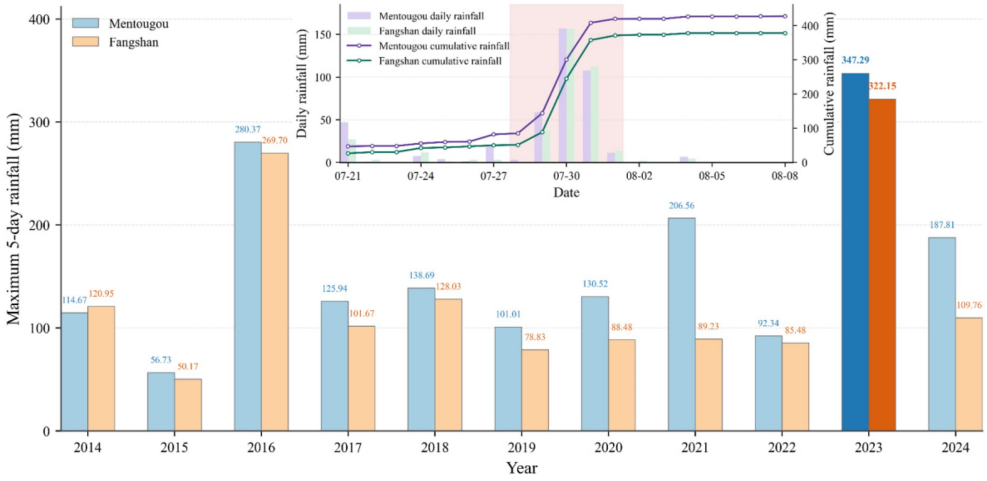

Figure 10. Annual maximum consecutive five-day precipitation totals at Mentougou and Fangshan stations during 2014–2024. Blue and orange bars represent Mentougou and Fangshan stations, respectively, with darker colors highlighting the 2023 values. The inset shows daily and cumulative precipitation around the July 2023 extreme rainfall event. Purple and green represent Mentougou and Fangshan stations, respectively. The shaded region highlights the extreme rainfall period.

3.4.2. Renewed LOS Deformation After Reduced Pre-Event Activity

Figures 11 and 12 show two representative landslides with declining pre-event activity. Between the radar acquisitions on 24 July and 5 August 2023, LOS displacement changed by −20.4 mm at landslide 1 and −15.5 mm at landslide 2. This observation interval spans the July 2023 extreme rainfall event. Both landslides showed changes in deformation after the event.

At landslide 1, cumulative LOS displacement gradually declined to approximately −110 mm between 2015 and 2021. It then remained mainly between −100 and −115 mm until the "23·7" event. Across two consecutive pre-event years, the fitted LOS rate changed from −20.4 to −2.9 mm yr^{-1}, while net displacement changed from −25.9 to −1.0 mm. The displacement curve gradually flattened, indicating a marked decline in LOS activity at this point before the event. After the event, cumulative LOS displacement rapidly declined to approximately −170 mm and reached approximately −200 mm by the end of monitoring. The fitted rate during the first six post-event months was −49.7 mm yr^{-1}, exceeding the final pre-event year's rate magnitude of 2.9 mm yr^{-1}. The short-term LOS rate, calculated through smoothing and local differentiation, reached a minimum near −300 mm yr^{-1}. These observations indicate clear renewed activity at this point.

Landslide 2 also experienced prolonged slow movement before the event. Cumulative LOS displacement remained near −60 mm before declining further to approximately −80 mm after the event. At this point, the fitted rate changed from +2.3 mm yr^{-1} during the pre-event year to −14.5 mm yr^{-1} during the first six post-event months. Negative LOS displacement accumulated after the event. Deformation increased again around the 2024 rainy season, with LOS displacement changing by −23.7 mm between 18 July and 11 August 2024. The fitted rate from 11 August 2024 to 3 April 2026 was −37.2 mm yr^{-1}, reflecting changes in movement between stages.

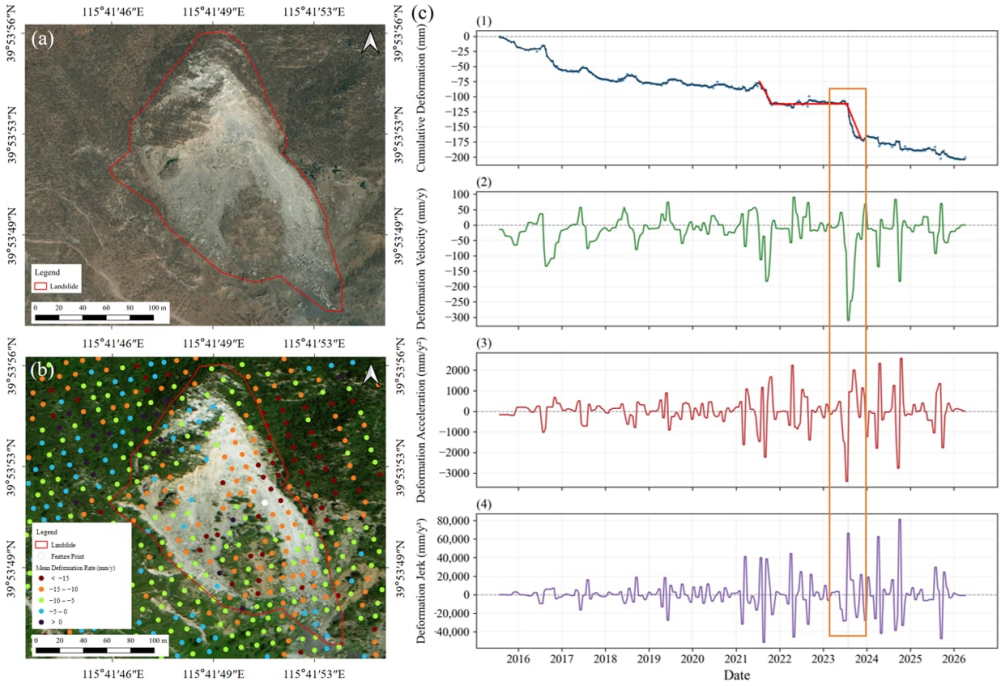

Figure 11. Optical imagery and InSAR kinematics for landslide 1 around the July 2023 event. (**a**) High-resolution pre-event optical image. (**b**) Post-event image and InSAR deformation rates. (**c**) Time series at an upper-source-area point: (**1**) cumulative LOS displacement (blue), (**2**) deformation rate (green), (**3**) acceleration (red), and (**4**) jerk (purple). Red line segments schematically illustrate stage-wise displacement trends. The orange box highlights the period around the July 2023 extreme rainfall event for visual comparison.

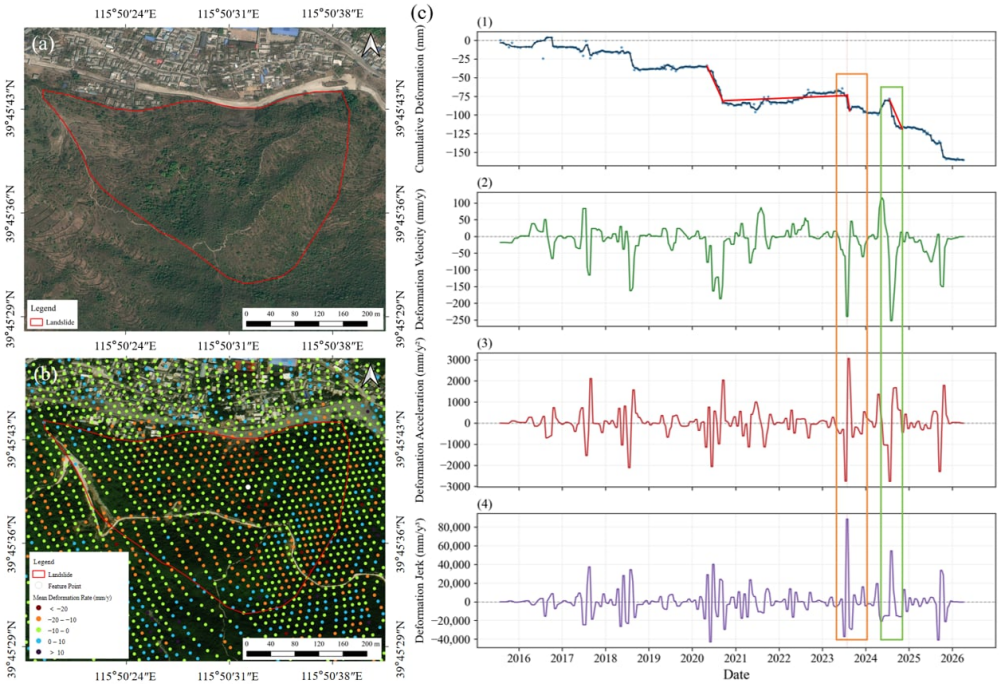

Figure 12. Optical imagery and InSAR kinematics for landslide 2 around the July 2023 event. (**a**) High-resolution pre-event optical image. (**b**) Post-event image and InSAR deformation rates. (**c**) Time series at an upper-source-area point: (**1**) cumulative LOS displacement (blue), (**2**) deformation rate (green), (**3**) acceleration (red), and (**4**) jerk (purple). Red line segments schematically illustrate stage-wise displacement trends. The orange and green boxes highlight the period around the July 2023 extreme rainfall event and a comparable rainy-season period in 2024, respectively.

Both cases experienced slow deformation earlier, followed by flatter displacement curves during the later pre-event period and renewed negative LOS displacement accumulation after the event. These observations indicate that declining pre-event activity does not imply a complete end to movement at pre-existing landslides. Continued post-event deformation monitoring therefore remains necessary.

At the plotted points for landslides 1 and 2, negative LOS rate enhancements were 46.8 and 16.8 mm yr^{-1}, respectively. Both approximate 95% confidence intervals exceeded zero, and both comparisons met the 0.05 significance criterion after Holm correction across the four cases (Table S4). For landslides 1 and 2, median 95% perturbation-interval half-widths across the complete histories were 42.6 and 40.2 mm yr^{-1} for velocity, respectively. Corresponding values were 926 and 873 mm yr^{-2} for acceleration, and 22,881 and 21,895 mm yr^{-3} for jerk.

3.4.3. Increased LOS Deformation at Continuously Active Slopes

Figures 13 and 14 show LOS deformation at landslides 3 and 4 before and after the extreme rainfall event. Both landslides maintained long-term slow movement before the event, and their cumulative displacement curves showed no clear prolonged plateau. This differs from the declining pre-event activity at the first two cases. During the first six post-event months, fitted LOS rates at both representative points became substantially more negative than during the pre-event year.

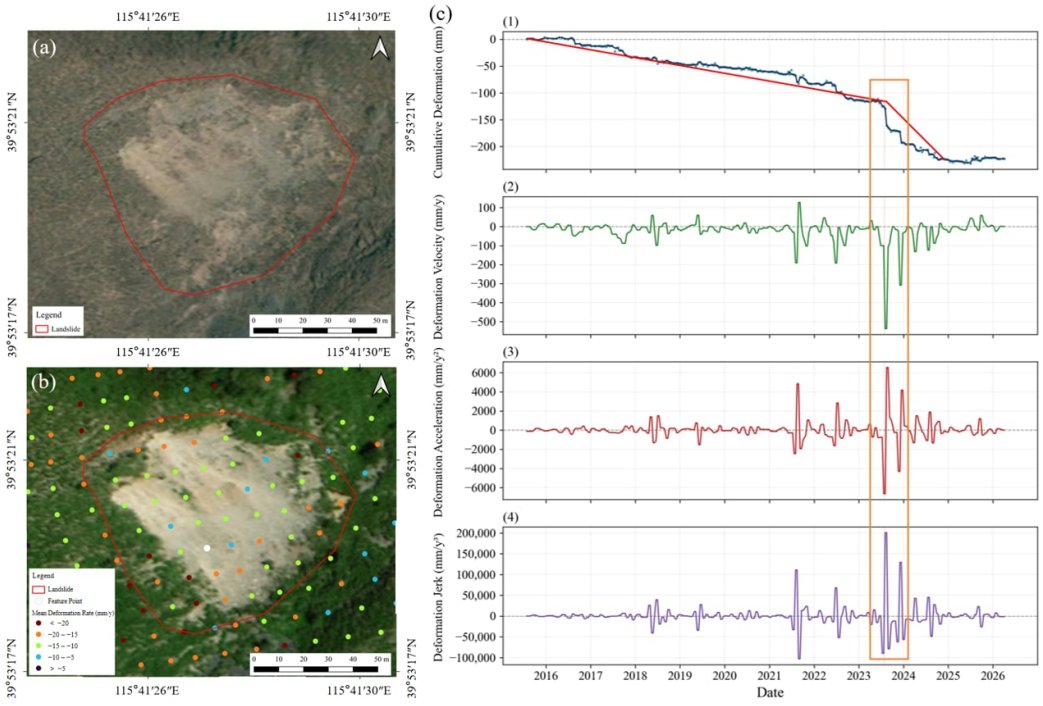

Figure 13. Optical imagery and InSAR kinematics for landslide 3 around the July 2023 event. (**a**) High-resolution pre-event optical image. (**b**) Post-event image and InSAR deformation rates. (**c**) Time series at an upper-source-area point: (**1**) cumulative LOS displacement (blue), (**2**) deformation rate (green), (**3**) acceleration (red), and (**4**) jerk (purple). Red line segments schematically illustrate stage-wise displacement trends. The orange box highlights the period around the July 2023 extreme rainfall event for visual comparison.

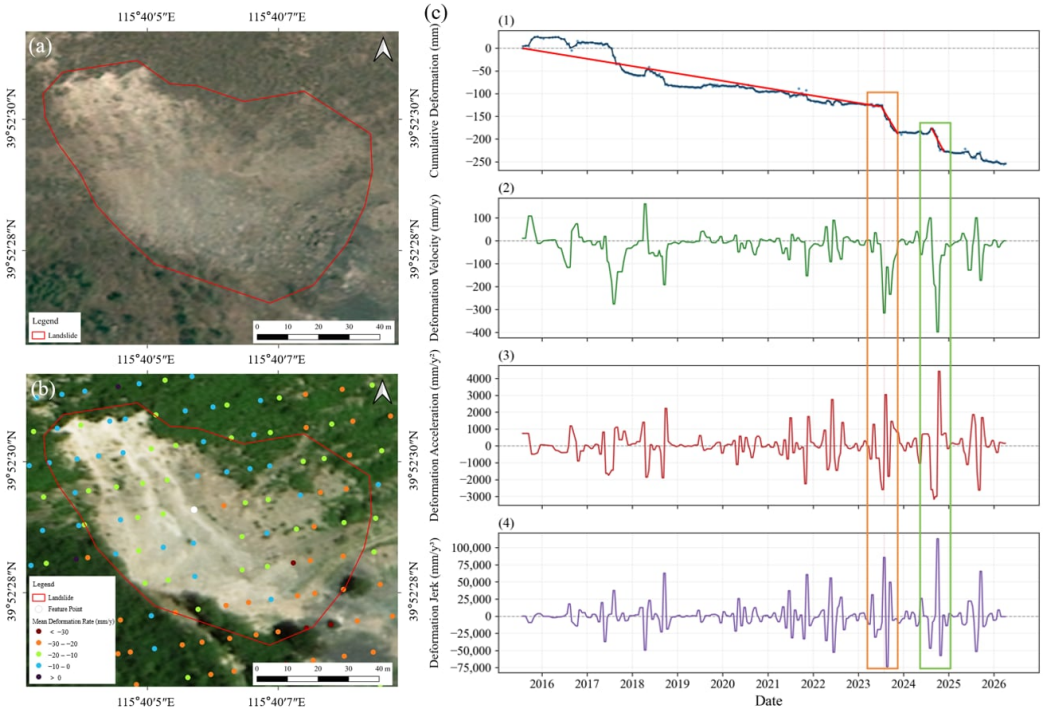

Figure 14. Optical imagery and InSAR kinematics for landslide 4 around the July 2023 event. (**a**) High-resolution pre-event optical image. (**b**) Post-event image and InSAR deformation rates. (**c**) Time series at an upper-source-area point: (**1**) cumulative LOS displacement (blue), (**2**) deformation rate (green), (**3**) acceleration (red), and (**4**) jerk (purple). Red line segments schematically illustrate stage-wise displacement trends. The orange and green boxes highlight the period around the July 2023 extreme rainfall event and a comparable rainy-season period in 2024, respectively.

At landslide 3, cumulative LOS displacement reached approximately −120 mm before the event, with a long-term mean rate of approximately −15 to −20 mm yr^{-1}. Fitted LOS rates over two consecutive pre-event years were −17.8 and −16.6 mm yr^{-1}, with net displacements of −19.4 and −25.0 mm, respectively. These observations indicate continued slow movement at the representative point before the event. After the event, cumulative LOS displacement declined further to approximately −200 mm and subsequently reached approximately −230 mm. The fitted rate during the first six post-event months reached −96.9 mm yr^{-1}, with a substantially larger magnitude than in the final pre-event year. This change indicates a phase of faster movement following continued slow deformation.

Landslide 4 also showed long-term movement before the event, with no clear plateau in its cumulative LOS displacement curve. After the event, cumulative displacement declined from approximately −120 to −190 mm. The representative point's fitted LOS rate changed from −7.5 mm yr^{-1} during the pre-event year to −75.1 mm yr^{-1} during the first six post-event months. The corresponding net displacements were −7.4 and −28.8 mm, respectively. The larger post-event negative rate magnitude indicates a phase of accelerated deformation at this point following continued movement. Around the 2024 rainy season, the displacement curve entered another declining phase. Cumulative LOS displacement reached approximately −240 mm later in the monitoring period, further illustrating changes in movement between stages.

Both landslides maintained slow movement before the extreme rainfall event and showed stronger negative LOS deformation afterward. Their histories indicate accelerated movement following continued activity. The time series at landslides 3 and 4 suggest that continuously active landslides may undergo substantial phases of acceleration after extreme rainfall events. Long-term InSAR observations can support continued assessment of their activity.

At the plotted points for landslides 3 and 4, negative LOS rate enhancements were 80.3 and 67.6 mm yr^{-1}, respectively. Both approximate 95% confidence intervals exceeded zero, and both comparisons met the 0.05 significance criterion after Holm correction across the four cases (Table S4). For landslides 3 and 4, median 95% perturbation-interval half-widths across the complete histories were 46.2 and 43.8 mm yr^{-1} for velocity, respectively. Corresponding values were 996 and 945 mm yr^{-2} for acceleration, and 25,158 and 23,584 mm yr^{-3} for jerk.

3.5. Spatial Patterns of Event-Related Shallow Landslides

The mean mapped polygon area was about 501 m^2. Count and area kernel densities showed similar hotspots in northern and eastern Mentougou and southwestern Fangshan (Figure 15). Peak densities reached 56.6 landslides km^{-2} and 7.34×10^4 m^2 km^{-2}, respectively. Some count hotspots had less pronounced area densities.

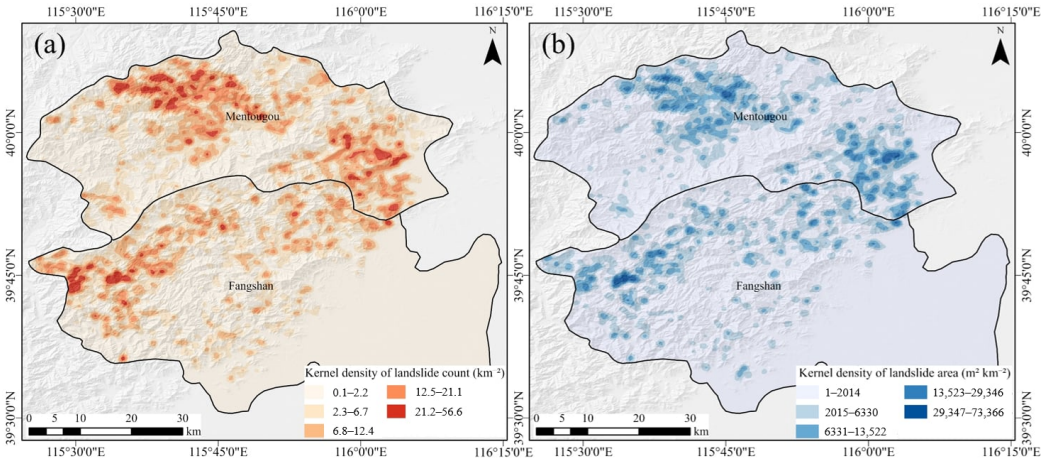

Figure 15. Spatial clustering of shallow landslides associated with the July 2023 rainfall event: (**a**) count-based kernel density (km^{-2}); (**b**) area-based kernel density (m^2 km^{-2}).

We selected eight topographic factors: elevation, slope, aspect, relief amplitude, topographic wetness index (TWI), topographic position index (TPI), profile curvature, and tangential curvature. Figure 16 shows the landslide counts and area proportions across different terrain classes.

Landslides mainly occurred at elevations of 200–900 m, slopes of 15–35°, and relief amplitudes of 250–450 m, representing 80.40%, 67.22%, and 64.63% of total landslide counts, respectively. Relatively high counts also occurred at TWI values of 4–7, TPI values of −75 to 25 m, and low absolute curvature, while northeast-, east-, and southeast-facing slopes contained relatively more mapped failures.

Table S3 adjusts landslide counts for the area of each terrain class. The count-to-area ratios were 1.71 at 400–500 m elevation and 1.44 at slopes of 20–25°. The TPI class from −25 to 0 m had the most landslides but a ratio of 0.76. Using slopes of at least 15° as the denominator, Fangshan and Mentougou had 450.22 and 590.06 shallow landslides per 100 km^2, respectively.

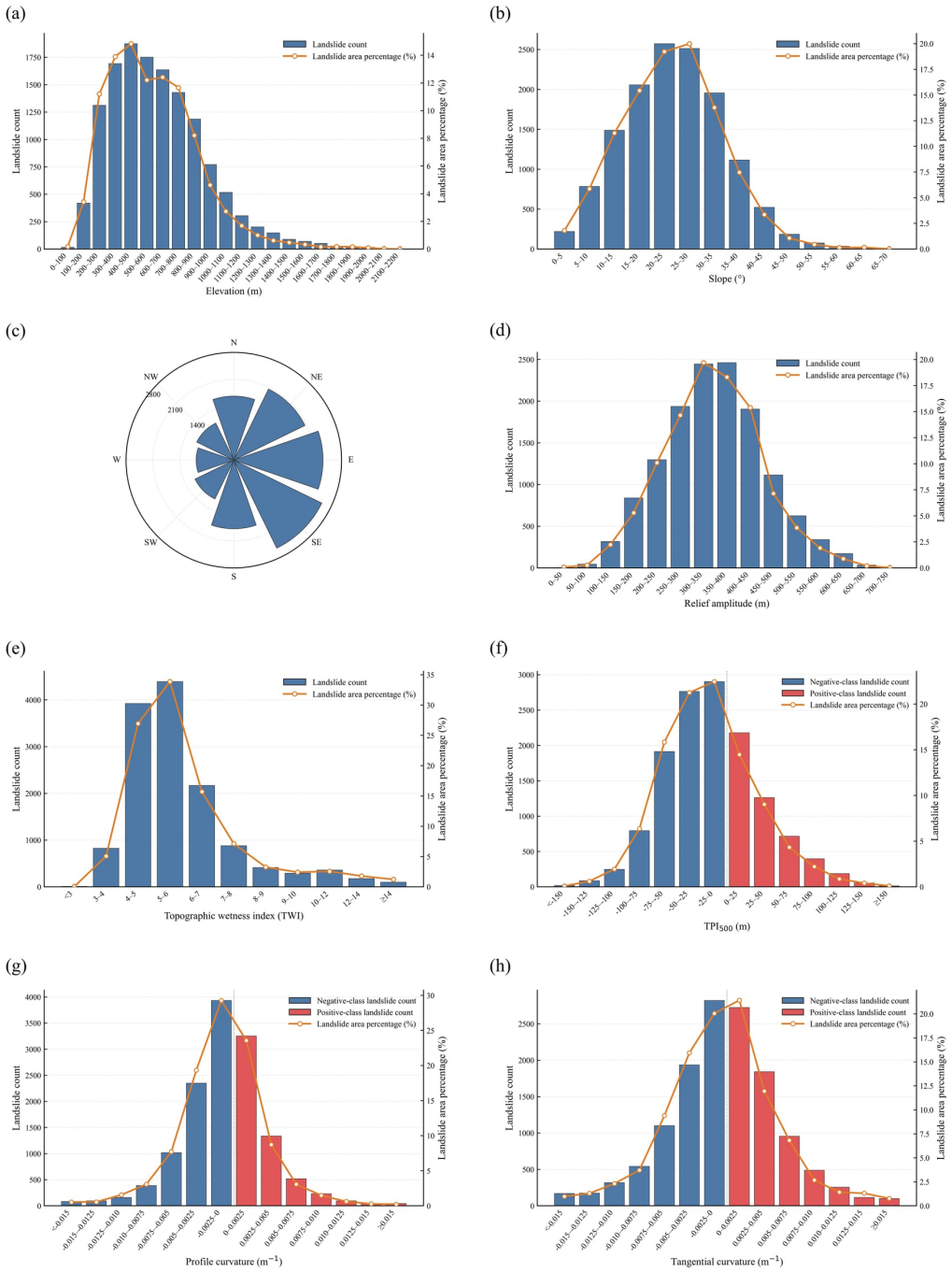

Figure 16. Distribution of shallow landslide counts and area percentages across topographic factor classes: (**a**) elevation; (**b**) slope; (**c**) aspect; (**d**) relief amplitude; (**e**) topographic wetness index (TWI); (**f**) topographic position index (TPI); (**g**) profile curvature; (**h**) tangential curvature.

4. Discussion

4.1. Complementary Remote Sensing Evidence for Landslide Activity

Each sensor contributes a different observation. Optical imagery captures new surface disturbance, InSAR tracks local LOS displacement, and LiDAR reveals landforms under vegetation. Differences among the maps can reflect the observation dates, sensor coverage and the type of feature each sensor detects.

4.2. Limitations and Future Directions

InSAR measures the projection of surface movement along the radar line of sight. Vegetation decorrelation, layover, radar shadow, and residual atmospheric or phase-unwrapping errors can limit the observations. The selected measurement points represent local deformation, and absolute LOS accuracy requires independent assessment. LiDAR interpretation covers one vegetation-covered slope and depends on the visibility of landforms and manual interpretation. Clouds, haze, and shadows limit optical mapping. Patch-level metrics describe within-area performance following model selection on the validation set.

Our analysis of rainfall and landslide deformation mainly relies on the temporal correspondence between rainfall and changes in displacement histories. We did not establish quantitative relationships using groundwater levels, pore-water pressure, soil moisture, or the physical and mechanical properties of soil and rock. Direct observations remain insufficient to explain the processes linking rainfall infiltration, groundwater responses, and slope failure. Future studies could combine field monitoring with hydromechanical models to examine slope deformation responses to rainfall and the factors controlling them.

5. Conclusions

Using the '23·7' extreme rainfall event in Beijing as a case study, this work integrated time-series InSAR, bitemporal optical imagery, and airborne LiDAR. These data helped identify different landslide types and examine their deformation histories and activity evolution. The main conclusions are as follows:

(1) Manual interpretation of pre-event Sentinel-1 LOS time series, optical imagery and geomorphic evidence delineated 102 slow-moving landslides covering about 6.59 km^2. The interpreted displacement histories supported labels of continuously active (86) and previously active with a trend toward stabilization (16). The labels refer to pre-event behavior inferred from the available observations.

(2) Adding pre-event imagery improved segmentation on the shared validation set. The six-channel U-Net achieved an F1-score of 94.13% and an IoU of 88.91%, exceeding the post-event-only model by 3.05 and 5.28 percentage points. Applying a 10 m^2 minimum mapping unit and manually checking the six-channel predictions by visual interpretation yielded 13,534 event-related shallow landslides covering about 6.77 km^2.

(3) The six-month screen identified acceleration at 50 CA landslides and renewed motion at 15 PS landslides. The other 37 did not meet either criterion. These observations support continued deformation monitoring of pre-existing landslides.

Supplementary Materials: The following supporting information can be downloaded at https://www.mdpi.com/article/10.3390/rs18234087/s1. Table S1: Pre-event slow-moving landslide inventory for Fangshan and Mentougou Districts, Beijing; Table S2: Short-window LOS displacement and rate by landslide; Table S3: Shallow-landslide counts adjusted by terrain availability; Table S4: Fitted LOS rate changes at the four plotted case points.

Author Contributions: Conceptualization, Y.Z. and D.Y.; methodology, validation, formal analysis, investigation, data curation, visualization, and writing—original draft preparation, X.W. and Y.Z.; software, X.W.; resources, Y.Z., D.Y., B.Z. and J.L.; writing—review and editing, X.W., Y.Z., and D.Y.; supervision and project administration, D.Y., B.Z. and J.L.; funding acquisition, D.Y. All authors have read and agreed to the published version of the manuscript.

Funding: This research was funded by the National Natural Science Foundation of China (grant number 52674248).

Data Availability Statement: Sentinel-1 SAR data are publicly available from the Copernicus Data Space Ecosystem (https://dataspace.copernicus.eu/, accessed on 29 October 2026), and SRTM DEM data from USGS EarthExplorer (https://earthexplorer.usgs.gov/, accessed on 29 October 2026). Other

datasets were provided by the Beijing Institute of Surveying and Mapping and are subject to the data provider's access restrictions.

Acknowledgments: The authors are grateful for the support from the project entitled "Research on the Mechanisms of Decoupled Mapping between Visual Appearance and Physical Deformation and the Prediction of Slope Dynamics in Open-Pit Mining Areas". The authors also thank the Beijing Institute of Surveying and Mapping for providing the research data. The authors appreciate the constructive comments and valuable suggestions from the reviewers and editors, which helped improve the quality of this manuscript.

Conflicts of Interest: The authors declare no conflicts of interest.

References

1. Myhre, G.; Alterskjær, K.; Stjern, C.W.; Hodnebrog, Ø.; Marelle, L.; Samset, B.H.; Sillmann, J.; Schaller, N.; Fischer, E.; Schulz, M.; et al. Frequency of extreme precipitation increases extensively with event rareness under global warming. *Sci. Rep.* **2019**, *9*, 16063. [CrossRef] [PubMed]
2. Gariano, S.L.; Guzzetti, F. Landslides in a changing climate. *Earth-Sci. Rev.* **2016**, *162*, 227–252. [CrossRef]
3. Zhang, Q.Y. Causes and implications of the extraordinary '23·7' rainstorm disaster in Fangshan District, Beijing. *China Flood Drought Manag.* **2023**, *33*, 43–47. (In Chinese)
4. Guo, Y.; Shen, J.; Liu, X.X.; Zhou, L.; Shi, X.F.; Wang, C.Y. Characteristics and spatial distribution of geological hazards triggered by the '23·7' extreme rainstorm in Mentougou District, Beijing. *China Flood Drought Manag.* **2025**, *35*, 39–45. (In Chinese)
5. Ma, H.; Wang, F. Inventory of shallow landslides triggered by extreme precipitation in July 2023 in Beijing, China. *Sci. Data* **2024**, *11*, 1083. [CrossRef] [PubMed]
6. Bontemps, N.; Lacroix, P.; Larose, E.; Jara, J.; Taipe, E. Rain and small earthquakes maintain a slow-moving landslide in a persistent critical state. *Nat. Commun.* **2020**, *11*, 780. [CrossRef] [PubMed]
7. Tu, G.X.; Huang, D.; Deng, H. Reactivation of a huge ancient landslide by surface water infiltration. *J. Mt. Sci.* **2019**, *16*, 806–820. [CrossRef]
8. Zhao, C.; Lu, Z. Remote sensing of landslides—A review. *Remote Sens.* **2018**, *10*, 279. [CrossRef]
9. Yang, Z.Q.; Qi, W.W.; Xu, C.; Shao, X.Y. Exploring deep learning for landslide mapping: A comprehensive review. *China Geol.* **2024**, *7*, 330–350. [CrossRef]
10. Zhang, Q.; Wang, T. Deep learning for exploring landslides with remote sensing and geo-environmental data: Frameworks, progress, challenges, and opportunities. *Remote Sens.* **2024**, *16*, 1344. [CrossRef]
11. Yang, Y.; Miao, Z.; Li, X.; Zhang, H.; Chen, S. LSL-SS-Net: Level set loss-guided semantic segmentation networks for landslide extraction. *GISci. Remote Sens.* **2024**, *61*, 2416727. [CrossRef]
12. Wang, X.; Zhong, D.; Liu, C.; Song, X.; Xu, L.; Deng, Y.; Li, S. DS Net: A dual-coded segmentation network leveraging large model prior knowledge for intelligent landslide extraction. *Remote Sens.* **2025**, *17*, 1912. [CrossRef]
13. Zhao, Z.; Tan, S.; Yang, Y.; Zhang, Q. Landslide identification from post-earthquake high-resolution remote sensing images based on ResUNet-BFA. *Remote Sens.* **2025**, *17*, 995. [CrossRef]
14. Cheng, Y.; Pang, H.; Li, Y.; Fan, L.; Wei, S.; Yuan, Z.; Fang, Y. Applications and advancements of spaceborne InSAR in landslide monitoring and susceptibility mapping: A systematic review. *Remote Sens.* **2025**, *17*, 999. [CrossRef]
15. Li, S.; Xu, W.; Li, Z. Review of the SBAS InSAR time-series algorithms, applications, and challenges. *Geod. Geodyn.* **2022**, *13*, 114–126. [CrossRef]
16. Xu, Q.; Zhao, B.; Dai, K.; Dong, X.; Li, W.; Zhu, X.; Yang, Y.; Xiao, X.; Wang, X.; Huang, J.; et al. Remote sensing for landslide investigations: A progress report from China. *Eng. Geol.* **2023**, *321*, 107156. [CrossRef]
17. Han, L.; Duan, P.; Liu, J.; Li, J. Research on landslide trace recognition by fusing UAV-based LiDAR DEM multi-feature information. *Remote Sens.* **2023**, *15*, 4755. [CrossRef]
18. Albanwan, H.; Qin, R.; Liu, J.K. Remote sensing-based 3D assessment of landslides: A review of the data, methods, and applications. *Remote Sens.* **2024**, *16*, 455. [CrossRef]
19. Yu, W.; Li, W.; Wu, Z.; Lu, H.; Xu, Z.; Wang, D.; Dong, X.; Li, P. Integrated remote sensing investigation of suspected landslides: A case study of the Genie slope on the Tibetan Plateau, China. *Remote Sens.* **2024**, *16*, 2412. [CrossRef]
20. Ren, Q.; Han, W. Review of landslide identification based on multisource data fusion. *Nat. Hazards Rev.* **2026**, *27*, 03126006. [CrossRef]
21. Casagli, N.; Intrieri, E.; Tofani, V.; Gigli, G.; Raspini, F. Landslide detection, monitoring and prediction with remote-sensing techniques. *Nat. Rev. Earth Environ.* **2023**, *4*, 51–64. [CrossRef]

22. Xu, Q.; Guo, C.; Dong, X.; Li, W.; Lu, H.; Fu, H.; Liu, X. Mapping and characterizing displacements of landslides with InSAR and airborne LiDAR technologies: A case study of Danba County, Southwest China. *Remote Sens.* **2021**, *13*, 4234. [CrossRef]
23. People's Government of Fangshan District, Beijing. Overview of Fangshan. 2 April 2026. Available online: https://www.beijing.gov.cn/renwen/bjgk/fsgk/sy/202604/t20260402_4573408.html (accessed on 28 October 2026). (In Chinese)
24. People's Government of Mentougou District, Beijing. Overview of Mentougou. 10 April 2023. Available online: https://www.beijing.gov.cn/renwen/bjgk/mtggk/sy/202304/t20230410_2994399.html (accessed on 28 October 2026). (In Chinese)
25. Yu, F.C.; Yan, Y.C.; Li, L.Y.; Huang, J.L.; Hu, C.; Xu, Y.J.; Tong, X.W. Assessment of geological hazard resilience in Beijing. *J. Beijing Norm. Univ. (Nat. Sci.)* **2023**, *59*, 306–312. (In Chinese)
26. Mao, S.L.; Liang, Z.; Shi, Y.; Yan, Y.; Fu, Y.; Wang, S. Influence of geological background on land resources utilization in the Western Mountain Areas of Beijing. *J. China Agric. Univ.* **2020**, *25*, 1–10. (In Chinese) [CrossRef]
27. Fangshan District Development and Reform Commission, Beijing. Planning for Comprehensive Ecological and Environmental Management Projects in Fangshan District (2006–2010). 7 September 2010. Available online: https://www.bjfsh.gov.cn/zwgk/ghjh/201009/t20100907_319953_fs.shtml (accessed on 29 October 2026). (In Chinese)
28. He, J.R.; Xu, S.Z.; Song, Q.W.; Hao, C.Y.; Dong, Y.; Ran, S.H.; Wu, J.Y.; Yu, Z.L.; Zheng, Y.L.; Sun, M. Characteristics and evolution of geoheritages in Mentougou District in the Xishan area, Beijing. *Hydrogeol. Eng. Geol.* **2024**, *51*, 210–221. (In Chinese) [CrossRef]
29. Yan, C.; Han, Y.; Zhao, Y.; Jiao, R.; Guo, X.; Ma, X.; Ma, C.; Wu, J.; Zhang, X. Improved Mask R-CNN Inventory Mapping and Multivariable Geo-Environmental Assessment of Rainfall-Induced Shallow Landslides in Mountainous Beijing, China. *Environ. Earth Sci.* **2026**, *85*, 463. [CrossRef]
30. Li, X.L.; Chen, T.; Zhao, W.; Chen, Y.; Fu, J.L.; Xu, X.H.; Shi, Y.; Shen, Y. Observational analysis of the influence of fine-scale Taihang Mountain topography on the extreme '23·7' rainfall in northern China. *Chin. J. Atmos. Sci.* **2025**, *49*, 629–644. (In Chinese)
31. Chen, T.; Chen, Y.; Fang, C.; Dong, L.; Fu, J.L.; Li, X.L.; Chen, S.; Shi, Y.; Shen, Y.; Xu, X.H.; et al. Fine characteristics of the July 2023 extreme rainfall in North China and associated synoptic weather patterns. *Acta Meteorol. Sin.* **2024**, *82*, 600–614. (In Chinese) [CrossRef]
32. Zhao, X.W.; Wang, C.Y.; Wang, Y.J.; Ji, M.F.; Wang, M.R.; Wang, J.Y.; Tang, D.S.; Jin, Y.L.; Fan, Q.; Hu, Q. Investigation and assessment of the extraordinary '23·7' basin-wide flood in the Haihe River Basin, Beijing. *J. Beijing Norm. Univ. (Nat. Sci.)* **2024**, *60*, 632–640. (In Chinese)
33. Beijing Daily. Beijing Holds a Press Conference on Flood Control and Disaster Relief: Post-Disaster Reconstruction Plans and Flood Impacts. 2023. Available online: https://www.beijing.gov.cn/ywdt/yaowen/202308/t20230810_3219401.html (accessed on 29 October 2026). (In Chinese)
34. National Meteorological Information Center. Daily Surface Climate Dataset for China (Version 3.0). Available online: https://k.data.cma.cn/mekb/?r=site/themeData (accessed on 29 October 2026). (In Chinese)
35. Alaska Satellite Facility. ASF SAR Data Search API. Available online: https://docs.asf.alaska.edu/api/keywords/ (accessed on 29 October 2026).
36. Twenty-First Century Aerospace Technology Co., Ltd. Proprietary Satellite Remote Sensing Data Products: Beijing-2 Satellite Imagery. Available online: https://www.21at.com.cn/bjxlwxzswsjsjcp/ (accessed on 28 October 2026). (In Chinese)
37. European Space Agency. Sentinel-1 Mission. Available online: https://sentiwiki.copernicus.eu/web/s1-mission (accessed on 28 October 2026).
38. U.S. Geological Survey. USGS EROS Archive—Digital Elevation—Shuttle Radar Topography Mission (SRTM). 29 June 2018. Available online: https://www.usgs.gov/centers/eros/science/usgs-eros-archive-digital-elevation-shuttle-radar-topography-mission-srtm (accessed on 29 October 2026).
39. Berardino, P.; Fornaro, G.; Lanari, R.; Sansosti, E. A new algorithm for surface deformation monitoring based on small baseline differential SAR interferograms. *IEEE Trans. Geosci. Remote Sens.* **2002**, *40*, 2375–2383. [CrossRef]
40. Lanari, R.; Mora, O.; Manunta, M.; Mallorqui, J.J.; Berardino, P.; Sansosti, E. A small-baseline approach for investigating deformations on full-resolution differential SAR interferograms. *IEEE Trans. Geosci. Remote Sens.* **2004**, *42*, 1377–1386. [CrossRef]
41. Gabriel, A.K.; Goldstein, R.M.; Zebker, H.A. Mapping small elevation changes over large areas: Differential radar interferometry. *J. Geophys. Res. Solid Earth* **1989**, *94*, 9183–9191. [CrossRef]
42. Lei, T.; Zhang, Y.; Lv, Z.; Li, S.; Liu, S.; Nandi, A.K. Landslide inventory mapping from bitemporal images using deep convolutional neural networks. *IEEE Geosci. Remote Sens. Lett.* **2019**, *16*, 982–986. [CrossRef]
43. Ronneberger, O.; Fischer, P.; Brox, T. U-Net: Convolutional Networks for Biomedical Image Segmentation. In *Medical Image Computing and Computer-Assisted Intervention (MICCAI 2015)*; Navab, N., Hornegger, J., Wells, W.M., Frangi, A.F., Eds.; Springer International Publishing: Cham, Switzerland, 2015; pp. 234–241. [CrossRef]
44. Liu, P.; Wei, Y.; Wang, Q.; Chen, Y.; Xie, J. Research on post-earthquake landslide extraction algorithm based on improved U-Net model. *Remote Sens.* **2020**, *12*, 894. [CrossRef]
45. Amankwah, S.O.Y.; Wang, G.; Gnyawali, K.; Hagan, D.F.T.; Sarfo, I.; Zhen, D.; Nooni, I.K.; Ullah, W.; Duan, Z. Landslide detection from bitemporal satellite imagery using attention-based deep neural networks. *Landslides* **2022**, *19*, 2459–2471. [CrossRef]

46. Jaboyedoff, M.; Oppikofer, T.; Abellán, A.; Derron, M.H.; Loye, A.; Metzger, R.; Pedrazzini, A. Use of LIDAR in landslide investigations: A review. *Nat. Hazards* **2012**, *61*, 5–28. [CrossRef]
47. van den Eeckhaut, M.; Poesen, J.; Verstraeten, G.; Vanacker, V.; Nyssen, J.; Moeyersons, J.; van Beek, L.P.H.; Vandekerckhove, L. Use of LIDAR-derived images for mapping old landslides under forest. *Earth Surf. Process. Landf.* **2007**, *32*, 754–769. [CrossRef]
48. Terrasolid Ltd. TerraScan User Guide: Ground. Available online: https://terrasolid.com/guides/tscan/crground.html (accessed on 29 October 2026).
49. McKean, J.; Roering, J. Objective landslide detection and surface morphology mapping using high-resolution airborne laser altimetry. *Geomorphology* **2004**, *57*, 331–351. [CrossRef]
50. Highland, L.M.; Bobrowsky, P. *The Landslide Handbook—A Guide to Understanding Landslides*; U.S. Geological Survey Circular 1325; U.S. Geological Survey: Reston, VA, USA, 2008. [CrossRef]
51. QGIS Development Team. Heatmap (Kernel Density Estimation). *QGIS 3.44 User Guide*. Available online: https://docs.qgis.org/3.44/en/docs/user_manual/processing_algs/qgis/interpolation.html#heatmap-kernel-density-estimation (accessed on 29 October 2026).
52. GRASS Development Team. r.slope.aspect. *GRASS GIS User Manual*. Available online: https://grass.osgeo.org/grass-stable/manuals/r.slope.aspect.html (accessed on 29 October 2026).

Disclaimer/Publisher's Note: The statements, opinions and data contained in all publications are solely those of the individual author(s) and contributor(s) and not of MDPI and/or the editor(s). MDPI and/or the editor(s) disclaim responsibility for any injury to people or property resulting from any ideas, methods, instructions or products referred to in the content.